Journal of Nuclear Medicine, published on October 13, 2016 as doi:10.2967/jnumed.116.178947

4D MR and attenuation map generation in PET/MR imaging using 4D PET derived deformation matrices: a feasibility study for lung cancer applications

Hadi Fayad[1], Holger Schmidt[2], Thomas Küstner[2,3], Dimitris Visvikis[1]

[1] INSERM, UMR1101, LaTIM, CHRU Morvan, Université de Bretagne Occidentale, Brest, France

[2] Department of Radiology, University of Tübingen, Tübingen, Germany

[3] University of Stuttgart, Stuttgart, Germany

Corresponding author:

FAYAD Hadi

LaTIM, INSERM UMR1101,

CHRU Morvan, 2 avenue Foch,

29609 Brest Cedex, France

Tél: +33 (0)298-018-111

Fax: +33 (0)298-018-124

Email: fayad@univ-brest.fr

Word count: 4881.

Keywords: 4D PET/MR, respiratory motion correction, attenuation correction, image generation.

Short running title: 4D MR and attenuation map generation.

ABSTRACT

Respiratory motion may reduce accuracy in fusion of functional and anatomical images using combined Positron emission tomography / Magnetic resonance (PET/MR) systems. Methodologies for the correction of respiratory motion in PET acquisitions using such systems are mostly based on the use of respiratory synchronized MR acquisitions to derive motion fields. Existing approaches based on tagging acquisitions may introduce artifacts in the MR images, while motion model approaches require the acquisition of training datasets. The objective of this work was to investigate the possibility of generating 4D MR images and associated attenuation maps (AMs) from a single static MR image combined with motion fields obtained from simultaneously acquired 4D non-attenuation corrected (NAC) PET images. **Methods:** 4D PET/MR datasets were acquired for 11 patients on a simultaneous PET/MR system. The 4D PET datasets were retrospectively binned into 4 motion amplitude frames corresponding to the simultaneously acquired T1-weighted 4D MR images. A T1-weighted 3D MR sequence with Dixon-based fat-water separation was also acquired at end of expiration for PET attenuation correction (AC) purposes. All reconstructed 4D NAC PET images were then elastically registered to the single 'end-expiratory' NAC PET image. The derived motion fields were subsequently applied to the 'end-expiratory' frame of the acquired 4D MR volume and the AM derived from the Dixon MR images to generate respiratory synchronized MR images and corresponding AMs. **Results:** The accuracy of the proposed method was assessed by comparing the generated to the acquired images according to metrics such as overall correlation coefficients and distance differences for anatomical landmarks between the generated and acquired MR datasets. High correlation coefficients (0.93±0.03) and small differences (2.69±0.5mm) were obtained. Moreover, small tissue classification differences (2.23±0.68%) between the generated and 4D MR extracted AMs were observed. **Conclusion:** Our results confirm the feasibility of using 4D NAC PET images for accurate PET AC and respiratory motion correction in PET/MR, without the need for patient specific 4D MR acquisitions.

INTRODUCTION

PET/MR is a new imaging technique allowing for simultaneous acquisition of PET and MR images (*1*). Several challenges associated with the use of MR for the correction of different effects reducing overall PET image qualitative and quantitative accuracy such as scatter, attenuation, and partial volume effects, have been recently identified (*2*). Moreover, the fusion accuracy of functional and anatomical information may be compromised by patient respiratory motion (*3*). Developing and combining such correction approaches is a challenging issue. The scope of this work was to address such issues with a combination of attenuation and respiratory motion corrections.

Current methods for AC in the thoracic region include the use of a two-point Dixon acquisition (*4,5*) that can be exploited to classify tissues into two to four different classes (air, fat, soft tissue, lung), and assign for each class a dedicated attenuation factor. However this method omits the attenuation caused by bone structures. Other segmentation approaches based on the use of Ultra-short Time Echo MR sequences (*6,7*), to account for bone structures by classifying tissues into air, fat, soft tissue and bones, have been proposed. An alternative methodology consists of atlas based approaches (*8*) using a database of registered Computed Tomography (CT) and MR acquisitions. The challenge with such approaches concerns the ability of the trained model to handle the large variability of pathological structures, compared to the database included datasets.

Respiratory motion leads to a reduction of both quantitative and qualitative accuracy of PET images. Correction methodologies involve the use of gated PET frames that are of low signal to noise ratio since each frame contains only part of the counts available throughout the acquisition of a respiratory average PET study (*9*). More advanced correction approaches consist in either correcting for the motion in the image space (*10,11*) or incorporating motion parameters into the iterative reconstruction process to produce a single motion-compensated PET image (*11,12*). Motion parameters may be extracted from 4D MR images, which in principle can correspond

perfectly to PET frames in simultaneous PET/MR (*13*), using the temporal information during the MR acquisition and PET list mode datasets containing temporal information for each acquired coincidence. However, this theoretical co-registration of PET and MR data will in reality be compromised by imperfect shimming and/or differences in the durations of the PET and MR acquisition protocols. In addition, the acquisition of 4D MR datasets may not always be compatible with clinical PET/MR practice. On the other hand, the use of 4D pulse sequences and parallel reconstruction algorithms, are associated with a compromise between image quality and overall acquisition times. This compromise, which is also true for 3D MR acquisitions, becomes more complicated in the case of 4D MR given the longer acquisition times involved. Previously proposed solutions include the use of tagged MR acquisitions (*14*), which may however introduce artifacts reducing the diagnostic quality of acquired MR images. Alternative approaches consist in modeling respiratory motion by creating patient specific (*15*–*17*) or generic (*18*) motion models. These models estimate internal respiratory motion from dynamic 3D MR images, and relate this internal motion to surrogate measures extracted using data-driven techniques based on 2D/3D MR image navigators. A disadvantage of these models is the necessary large training datasets.

The main objective of this work is to generate 4D MR images and associated 4D AMs for PET motion correction using the combination of a single static MR image and deformation matrices obtained from simultaneously acquired 4D NAC PET images. A similar concept was previously proposed in 4D PET/CT imaging (*18*). The aim is to replace the lengthy 4D MR acquisitions (*13*-*17*) by a single static MR acquisition, and facilitate accurate 4D MR-based AC for the simultaneously acquired 4D PET datasets by generating MR image series that mimic 4D MR acquisitions. The availability of 4D AC PET respiratory gated images using in each respiratory frame the whole statistics acquired throughout the respiratory cycle is essential for certain applications, such as for example the use of PET/MR imaging in radiotherapy where the extent of whole tumor motion is necessary for the implementation of a 4D treatment protocol. The proposed approach was tested on 11 patients who underwent 4D PET/MR acquisitions on a Siemens

Biograph mMR PET/MR system.

MATERIALS AND METHODS

General Method Description

A prerequisite of the proposed approach is the availability of a dynamic respiratory synchronized PET image series and a unique 'end-expiratory' 3D MR volume. The proposed method aims at generating MR images and their corresponding AMs, associated with each PET respiratory synchronized frame, using a number of steps (Fig. 1): NAC respiratory gated PET frames are reconstructed and the one corresponding to the end-expiratory state is used as reference PET frame. The reference PET frame is registered to all NAC PET frames using a non-rigid registration algorithm to derive associated deformation matrices. These matrices are subsequently applied to either the acquired 'end-expiratory' MR volume to generate the corresponding respiration synchronized MRI frames, or to the AM extracted from the 'end-expiratory' 3D Dixon MR volume to generate 4D respiratory synchronized AMs.

Patient Datasets

11 consecutively enrolled patients with thoracic or upper abdomen lesions (bronchial, sigma and nasopharynx carcinoma) participated in the study (age 32-70 y; mean 58±11 y). Table 1 shows an overview of the patient demographics, including corresponding lesion characteristics. Patient datasets were acquired on a whole-body PET/MR (Biograph mMR; Siemens Healthcare, Erlangen, Germany), which combines a PET system with transaxial and axial fields of view of 59.4 cm and 25.8 cm respectively, and a 3T MR system. Phased-array body coils optimized for minimally 511-keV photon attenuation were used for signal detection. A T1-weighted spoiled gradient-echo sequence with Dixon-based fat-water separation was acquired at breath-hold (echo times 1.23 ms and 2.46 ms, repetition time 3.6 ms, flip angle 10°, resolution 2.6x2.6x2.6 mm,

bandwidth 965 Hz/px, parallel imaging acceleration factor 2, slices per slab 128, acquisition time 19s, end-expiratory position), and tissues were classified into air, lung, soft tissue, and adipose tissue to obtain an AM for the entire PET field of view (*5,19*). PET data of one bed position (covering thorax and upper abdomen) were subsequently recorded in list mode during 5 minutes under free breathing conditions. PET/MR scanning started without repeated radiotracer injection after routine PET/CT (124±11 min after injection of 336–371 MBq of 18F-FDG).

The 1D respiratory signal used for PET data binning was extracted from 2D MR navigator images of the diaphragm position (*13*). Finally, during the first 3 minutes of the PET scan, multiple sagittal 2D MR slices covering the PET field of view were acquired in order to obtain a 4D MR series for validation purposes (echo time 1.8 ms, repetition time 3.7 ms, flip angle 15°, resolution 2x2x10 mm^3, bandwidth 670 Hz/px, 36 slices per slab, acquisition time per image slice 0.4s; see (*13*) for more information). In order to reconstruct 4D MR series and to cover 1 respiratory cycle, 12 frames of each slice were acquired sequentially before moving to the next slice. 36 slice positions in the left-to-right direction were acquired covering patient's thorax and upper abdomen, resulting in approximately 10-mm resolution in this direction. This low resolution is acceptable considering low amplitude respiratory motion generally in this direction (*12*). The amplitude of the diaphragm position extracted from the MR navigator were used to define 4 respiratory gates by dividing the range between the 0.05 and 0.95 quantiles into 4 equally sized intervals (in order to reduce the influence of outliers). The mean temporal respiratory position within the respective gate interval was subsequently determined. Thus, for each slice and each gated list-mode frame, the MR image closest to the frame's mean temporal respiratory position was inserted into the corresponding 3D MR volume, and the remaining eleven 2D MR images were discarded for the specific temporal frame (*12*).

All patients provided written informed consent for participation in the 4D PET/MR study, which was approved by the local institutional review board.

Datasets Preparation

For every patient, the 4D PET acquired datasets were retrospectively binned into 4 motion amplitude frames corresponding to the simultaneously acquired 4D MR images and reconstructed using a 3D ordered subsets expectation maximization algorithm (*20,21*) with 3 iterations, 21 subsets, 5mm Gaussian filter, 1.78x1.78x2 mm voxel size without AC. The choice of 4 frames was based on previous work, where it was shown that for a 5 min PET acquisition with the mMR system, 4 amplitude binned gates resulted in superior lesion contrast, signal to noise ratio, and full width at half maximum results (FWHM) compared to the use of 6/8 gates (*13*).

Image Generation

All reconstructed 4D NAC PET images were registered to the single 'end-expiratory' NAC PET image corresponding to the 'end-expiratory' frame of the acquired 4D MR volume, using a B-splines based deformable registration algorithm (*22*), previously validated for use with PET (*23*). The influence of the PET image statistics in the registration results, showing negligible influence, was also previously evaluated (*24*).

The derived motion fields were subsequently applied to the 'end-expiratory' frame of the acquired 4D MR volume and the corresponding AM in order to generate respiratory synchronized MR images and corresponding AMs, respectively. When acquiring a single MR image for each patient, the synchronized respiratory signal can be used to determine the corresponding temporal and motion amplitude information. Subsequently, using the PET list mode data and these temporal/amplitude characteristics of the single acquired MR frame, a corresponding PET image can be reconstructed (reference PET frame).

To apply the motion fields to the single acquired MR frame (or the corresponding AM), f(x), it is necessary to approximate the B-spline coefficients derived from the non-rigid registration into discrete 3D voxel based displacement vector images. In order to avoid such approximations, the

MR frame, f(x), was instead represented using a 2-D spline interpolation as:

$$f(x) = \sum_{j \in Z^2} b_l \, \beta^r (x - l) \qquad (1)$$

where, $\beta^r(x)$ is a tensor product of centered B-splines of degree r and coefficient b_i is obtained from voxel values $f(i)$ through filtering in the rectangular domain Z^2. The set of 2-D spline interpolations can represent a 3D object corresponding to a MR frame. 2D-splines were chosen because they are the smoothest of all possible interpolating curves (such as polynomials) in the sense that it minimizes the integral of the square of the second derivative and has previously proved its superiority over other alternatives (*23*). Finally, the warped sequence $f(U(.))$ (acquired 4D MR or AM sequence) is generated by applying the deformation matrices $U_{r\text{-}s}$ (r and s corresponding to the reference and one of the respiratory synchronized PET NAC frames, respectively) to $f(x)$.

Image Analysis and Validation

The accuracy of the proposed method was assessed by comparing the generated 4D MR to the originally acquired 4D MR images. Regarding the AMs, we compared those generated using the proposed method and the corresponding ones extracted from the 4D MR series using the 3D Dixon MR sequence corresponding to the 'end-expiratory' PET frame as reference.

Local image analysis was performed using profiles placed across moving parts of the patient's anatomy such as the diaphragm. A qualitative global comparison was performed using difference images. For global quantitative estimation, we computed a correlation coefficient ρ, which measures a linear affine relationship between the intensities of the two compared images A and B:

$$\rho_{(A,B)} = \sum_a \sum_b \frac{(I_a - M_A)(I_b - M_B)}{\sqrt{\sigma_A}\sqrt{\sigma_B}} \quad (2)$$

where, I_a and I_b are intensities of voxels *a* of images A and voxels *b* of image B, respectively (0 < *a* < number of voxels of image A, 0 < *b* < number of voxels of image B), *M* and σ are the mean and standard deviation of the image intensities. The closer *ρ* is to 1, the stronger the positive correlation.

Finally, a validation based on landmark identification was performed (*25*). Two radiologists with more than 15 years' experience in MR imaging selected the same easily identifiable anatomical landmarks in both the acquired 4D MR images (ground-truth) and generated 4D MR volumes. The Euclidian Distance (ED) was subsequently calculated between each point in the reference volume and the warped MR volumes:

$$ED = \frac{1}{N}(\|q_k - r_k\|^2) \quad (3)$$

where, q_k and r_k are the coordinates of the *k-th* landmark in the acquired and generated MR images, respectively. *ED* is expressed in mm and N is the total number of anatomical landmarks considered. 13 landmarks were used covering different thoracic areas in order to investigate regions of interest characterized by variable magnitudes of motion due to respiration (*26*–*29*). These include right and left apex, aortic cross, sternum, carina, left and right nipple, left and right diaphragm high position and the "high, low, left and right" boundaries of the tumor (*30*).

In addition, a region of interest analysis in the lungs was used to compare the different AC PET images obtained using the original and warped 4D MR series and their corresponding AMs.

RESULTS

Fig. 2 shows an example of an acquired MRI (corresponding to the ground-truth) and a generated MRI. Profiles along the diaphragm (illustrated in the bottom of Fig. 2 for one patient)

indicate a good match between the acquired and generated 4D MR series.

Fig. 3 shows the difference images between an acquired and a generated MR image demonstrating small differences (-5 to +5 which represents differences of <2% given that images were normalized between 0 and 255). Considering the 11 patients, high correlation coefficients (overall mean±std of 0.93 ± 0.03) were measured between both series as shown in Table 2.

Finally, Fig. 4A shows the mean *ED* results and the corresponding standard deviations between acquired and corresponding generated MR images (for all respiratory phases of every patient). The mean *ED was* 2.69±0.5 mm with a maximum ED of 3.38 mm (box-and-whisker plot, Fig. 4B). Moreover, the repeatability results in identifying the internal anatomical landmarks revealed a mean intra-operator and inter-operator variability of <1.5mm, demonstrating good intra-operator agreement in the landmarks' identification.

Finally, the acquired MR series were used to create 4D respiratory synchronized AMs using a 2-point Dixon's approach. At each step we compared maps generated using our method and those extracted from the 4D MR series. Fig. 5 shows the axial, coronal and axial view of the generated AM (Fig. 5A), the corresponding 4D MR generated AM (Fig. 5B) and corresponding difference images (Fig. 5C) represented by a binary image where black (intensity=0) and white voxels (intensity=1) correspond to those who are correctly and wrongly classified respectively. As a result there was a high correlation between those maps generated using our method and those extracted from the 4D MR series (Table 3) with a mean correlation coefficient for all 11 patients of 0.93±0.05. Fig. 6A shows the percentage of the voxels that are misclassified with a mean error of 2.23 as presented by the box-and-whisker plot (Fig. 6B).

The region of interest analysis in the AC PET images, using the original and warped MR AMs for all patients, led to a mean difference of 2.65% with corresponding intensities (radioactivity concentration) of 18.22±3.16 and 17.39±3.85 MBq/mL for the original and warped based AMs respectively.

DISCUSSION

The goal of this paper was to investigate the feasibility of producing a 4D MR series from corresponding 4D NAC PET images and a single MR acquisition, thus eliminating the need for 4D MR acquisitions. 11 patient datasets were included in the validation. The generated and acquired MR series were highly correlated. These results demonstrate the ability of the proposed method to derive 4D MR frames from 4D NAC PET images' registration and one reference MR frame. In addition, the generated MR frames can create 4D AMs to improve MR based AC in 4D PET imaging in terms of correspondence between the two datasets (same motion characteristics). For all 11 patients, generated and acquired AMs were well correlated, as were the corresponding AC PET images obtained using these AMs. While this methodology was previously evaluated for PET/CT imaging (*24*), this study demonstrates that it is also applicable in PET/MR reducing the need of 4D MR acquisitions for 4D PET AC. In addition, within the context of PET/MR respiratory motion correction, this approach may resolve issues associated with the acquisition of motion monitoring specific MRI sequences (*16*), reducing the overall time available for clinically relevant MR data. The respiratory motion correction can be based on the use of the same deformation fields, used in this work for 4D MR and AM generation, either in the image space (*10*) or within the iterative reconstruction process to produce a single motion-compensated PET image (*12*). This approach allows therefore parallel attenuation and respiratory motion correction and may be compared to alternative methodologies based on patient specific (*15*–*17*) or generic (*18*) motion models relating internal respiratory motion from dynamic 3-D MR images to surrogate measures extracted using data-driven techniques based on 2D/3D MR image navigators.

A possible limitation of this study is that a unique level of PET image statistical quality was considered (5 minutes acquisition per bed position). However, in a previous study concerning PET/CT imaging (*24*), different levels of PET image statistical quality were considered and it was demonstrated that clinically relevant PET acquisition times (3 minutes per bed position) were sufficient for the implementation of such an approach. Another limitation in this study is the use of

a 2 point Dixon's approach for AC which omits the attenuation caused by bone structures. To resolve this issue, different approaches have been recently proposed such as the use of Ultra-short Time Echo MRI sequences (*31*), combining Ultra-short Time Echo sampling for bone detection and gradient echoes for Dixon water–fat separation in a radial 3-dimensional acquisition. However, given that the proposed approach can generate 4D MR images and corresponding AMs, it can be easily extended to take into account bones when using an Ultra-short Time Echo or alternative MRI sequences for PET AC purposes. Finally, a potential improvement of the proposed methodology would be the use of TOF PET acquisitions that may help improving the quality of NAC PET images and therefore improve the accuracy and robustness of corresponding deformation matrices.

CONCLUSIONS

This study demonstrates the feasibility of using 4D NAC PET images to derive matching 4D MR series and corresponding AMs from a single respiratory state MR image. The efficiency was assessed on 11 patient clinical datasets. Results demonstrate a high correlation between generated and acquired MR and corresponding AMs series, thus eliminating the need for long 4D MR acquisitions. Future work will consist of exploring the proposed approach in conjunction with respiratory motion models reducing the potential limitation of monitoring non-cyclic motion using only four respiratory gates used in this work.

References

1. Delso G, Fürst S, Jakoby B, et al. Performance measurements of the Siemens mMR integrated whole-body PET/MR scanner. *J Nucl Med.* 2011;52:1914-22.

2. Bailey DL, Antoch G, Bartenstein P, et al. Combined PET/MR: the real work has just started. Summary Report of the Third International Workshop on PET/MR Imaging; February 17–21, 2014, Tübingen, Germany. *Mol Imaging Biol.* 2015;17:297-312.

3. Brendle CB, Schmidt H, Fleischer S, Braeuning UH, Pfannenberg CA, Schwenzer NF. Simultaneously acquired MR/PET images compared with sequential MR/PET and PET/CT: alignment quality. *Radiology.* 2013;268:190-9.

4. Dixon WT. Simple proton spectroscopic imaging. *Radiology.* 1984;153:189-94.

5. Martinez-Möller A, Souvatzoglou M, Delso G, et al. Tissue classification as a potential approach for attenuation correction in whole-body PET/MRI: evaluation with PET/CT data. *J Nucl Med.* 2009;50:520-6.

6. Catana C, van der Kouwe A, Benner T, et al. Toward implementing an MRI-based PET attenuation-correction method for neurologic studies on the MR-PET brain prototype. *J Nucl Med.* 2010;51:1431-8.

7. Keereman V, Fierens Y, Broux T, Deene YD, Lonneux M, Vandenberghe S. MRI-based attenuation correction for PET/MRI using ultrashort echo time sequences. *J Nucl Med.* 2010;51:812-8.

8. Hofmann M, Steinke F, Scheel V, et al. MRI-based attenuation correction for PET/MRI: a novel approach combining pattern recognition and atlas registration. *J Nucl Med.* 2008;49:1875-83.

9. Bruyant P, Turzo A, Bizais Y, Cheze Le Rest C, Visvikis D. A comparison of three respiratory gating methods in PET imaging for oncology. *J Nucl Med.* 2006;47:183P-a.

10. Dawood M, Lang N, Jiang X, Schafers KP. Lung motion correction on respiratory gated 3-D PET/CT images. *IEEE Trans Med Imaging.* 2006;25:476-85.

11. Fayad H, Schmidt H, Würslin C, Visvikis D. Reconstruction incorporated respiratory motion correction in clinical simultaneous PET/MR imaging for oncology applications. *J Nucl Med.* 2015;56:884-9.

12. Lamare F, Ledesma Carbayo MJ, Cresson T, et al. List-mode-based reconstruction for respiratory motion correction in PET using non-rigid body transformations. *Phys Med Biol.* 2007;52:5187-204.

13. Würslin C, Schmidt H, Martirosian P, et al. Respiratory motion correction in oncologic PET using T1-weighted MR imaging on a simultaneous whole-body PET/MR system. *J Nucl Med.* 2013;54:464-71.

14. Guérin B, Cho S, Chun SY, et al. Nonrigid PET motion compensation in the lower abdomen using simultaneous tagged-MRI and PET imaging. *Med Phys.* 2011;38:3025-38.

15. Fayad H, Odille F, Schmidt H, et al. The use of a generalized reconstruction by inversion of coupled systems (GRICS) approach for generic respiratory motion correction in PET/MR imaging. *Phys Med Biol.* 2015;60:2529-46.

16. King AP, Buerger C, Tsoumpas C, Marsden PK, Schaeffter T. Thoracic respiratory motion estimation from MRI using a statistical model and a 2-D image navigator. *Med Image Anal.* 2012;16:252-64.

17. Dikaios N, Izquierdo-Garcia D, Graves MJ, Mani V, Fayad ZA, Fryer TD. MRI-based motion correction of thoracic PET: initial comparison of acquisition protocols and correction strategies suitable for simultaneous PET/MRI systems. *Eur Radiol.* 2012;22:439-46.

18. Fayad HJ, Buerger C, Tsoumpas C, Cheze-Le-Rest C, Visvikis D. A generic respiratory motion model based on 4D MRI imaging and 2D image navigators. In: 2012 IEEE Nuclear Science Symposium and Medical Imaging Conference (NSS/MIC). 2012. p. 4058-61.

19. Bezrukov I, Schmidt H, Gatidis S, et al. Quantitative evaluation of segmentation- and atlas-based attenuation correction for PET/MR on pediatric patients. *J Nucl Med.* 2015;56:1067-74.

20. Hudson HM, Larkin RS. Accelerated image reconstruction using ordered subsets of projection data. *IEEE Trans Med Imaging.* 1994;13:601-9.

21. Liu X, Comtat C, Michel C, Kinahan P, Defrise M, Townsend D. Comparison of 3-D reconstruction with 3D-OSEM and with FORE+OSEM for PET. *IEEE Trans Med Imaging.* 2001;20:804-14.

22. Ledesma-Carbayo MJ, Mahía-Casado P, Santos A, Pérez-David E, García-Fernández MA, Desco M. Cardiac motion analysis from ultrasound sequences using nonrigid registration: validation against Doppler tissue velocity. *Ultrasound Med Biol.* 2006;32:483-90.

23. Lamare F, Ledesma Carbayo MJ, Cresson T, et al. List-mode-based reconstruction for respiratory motion correction in PET using non-rigid body transformations. *Phys Med Biol.* 2007;52:5187-204.

24. Fayad HJ, Lamare F, Le Rest CC, Bettinardi V, Visvikis D. Generation of 4-dimensional CT images based on 4-dimensional PET-derived motion fields. *J Nucl Med.* 2013;54:631-8.

25. Sarrut D, Boldea V, Miguet S, Ginestet C. Simulation of four-dimensional CT images from deformable registration between inhale and exhale breath-hold CT scans. *Med Phys.* 2006;33:605-17.

26. Giraud P, Reboul F, Clippe S, et al. Respiration-gated radiotherapy: current techniques and potential benefits. *Cancer Radiother.* 2003;7:15s-25s.

27. Murphy MJ, Martin D, Whyte R, Hai J, Ozhasoglu C, Le Q-T. The effectiveness of breath-holding to stabilize lung and pancreas tumors during radiosurgery. *Int J Radiat Oncol Biol Phys.* 2002;53:475-82.

28. Ionascu D, Jiang SB, Nishioka S, Shirato H, Berbeco RI. Internal-external correlation investigations of respiratory induced motion of lung tumors. *Med Phys.* 2007;34:3893-903.

29. van Sörnsen de Koste JR, Lagerwaard FJ, Nijssen-Visser MRJ, Graveland WJ, Senan S. Tumor location cannot predict the mobility of lung tumors: a 3D analysis of data generated from multiple CT scans. *Int J Radiat Oncol Biol Phys.* 2003;56:348-54.

30. Fayad H, Pan T, Clement JF, Visvikis D. Technical note: Correlation of respiratory motion between external patient surface and internal anatomical landmarks. *Med Phys.* 2011;38:3157-64.

31. Berker Y, Franke J, Salomon A, et al. MRI-based attenuation correction for hybrid PET/MRI systems: a 4-class tissue segmentation technique using a combined ultrashort-echo-time/Dixon MRI sequence. *J Nucl Med.* 2012;53:796-804.

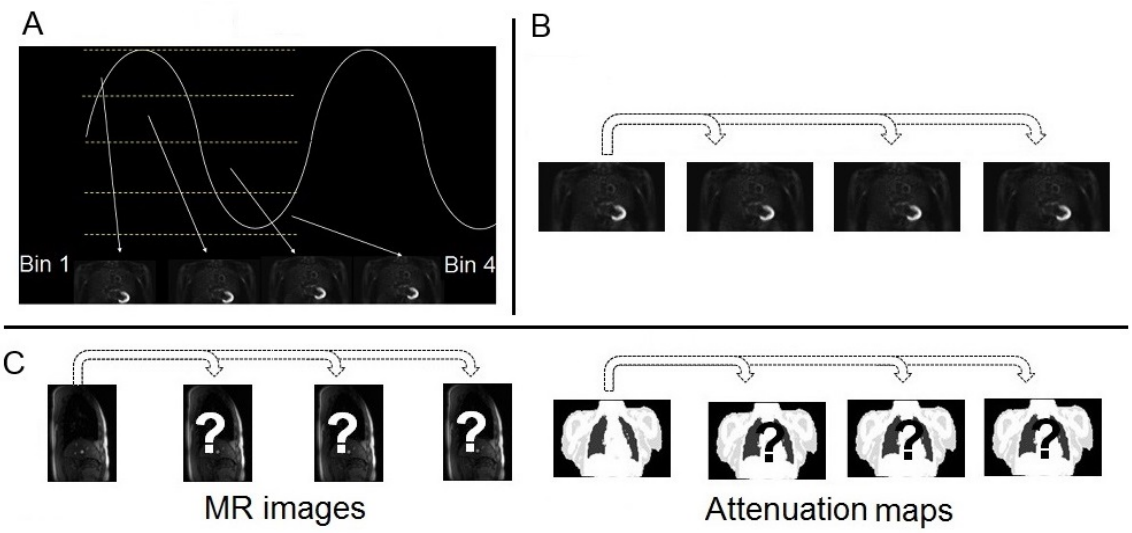

Figure 1: Workflow of the proposed method: (A) 4D NAC PET reconstruction and gating into 4 bins. (B) NAC PET bins registration to the reference ‘end of expiration’ bin. (C) Application of the obtained motion fields to the ‘end expiration’ 3D MR volume and Corresponding AMs.

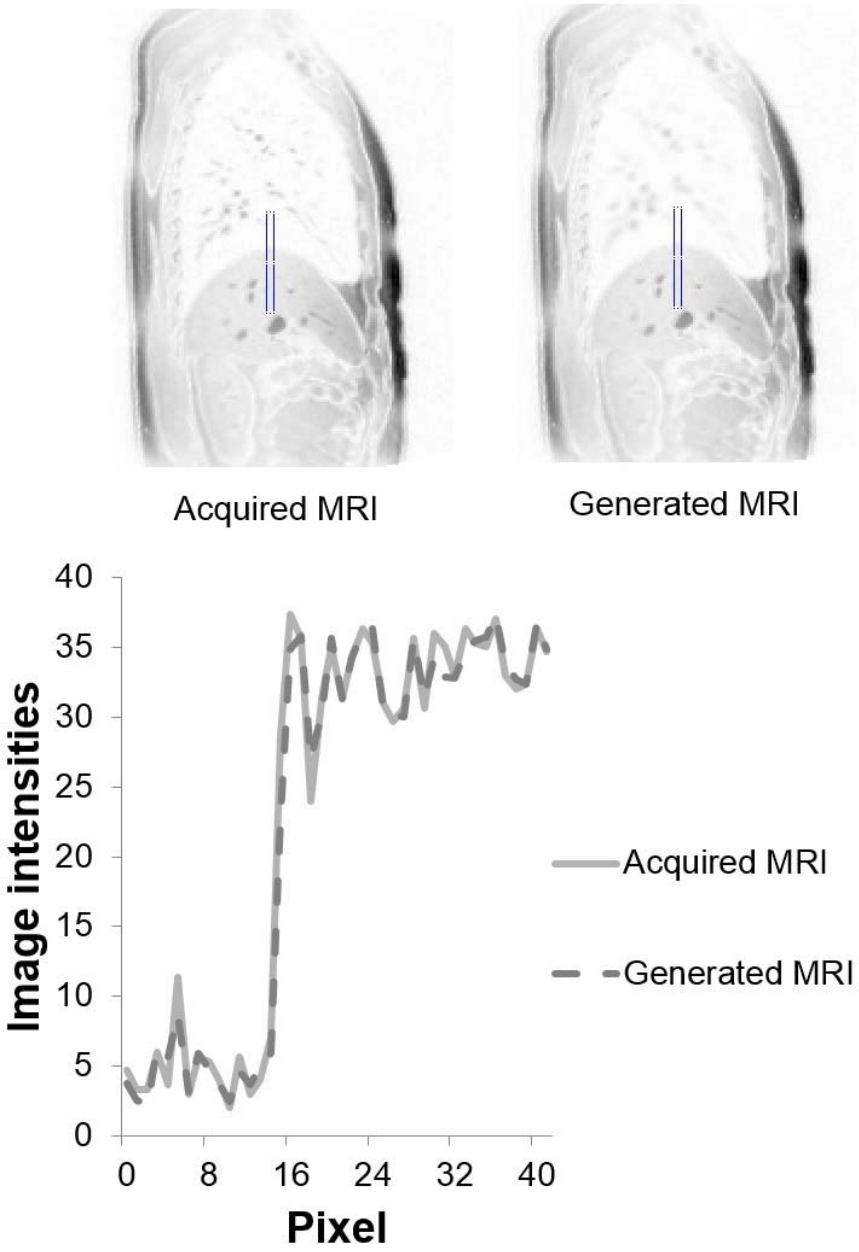

Figure 2: Profile drawn across the diaphragm on both the acquired and the generated MR images (MRI are shown in a sagittal view).

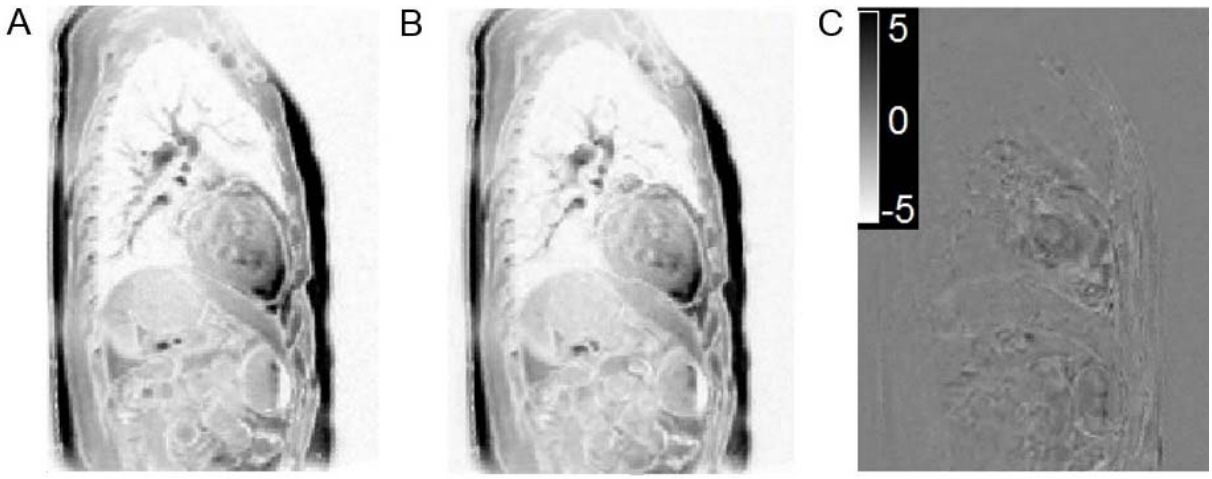

Figure 3: (A) The sagittal view of a slice of an acquired MR image. (B) Same slice of the corresponding generated MR image. (C) Difference image between the two images.

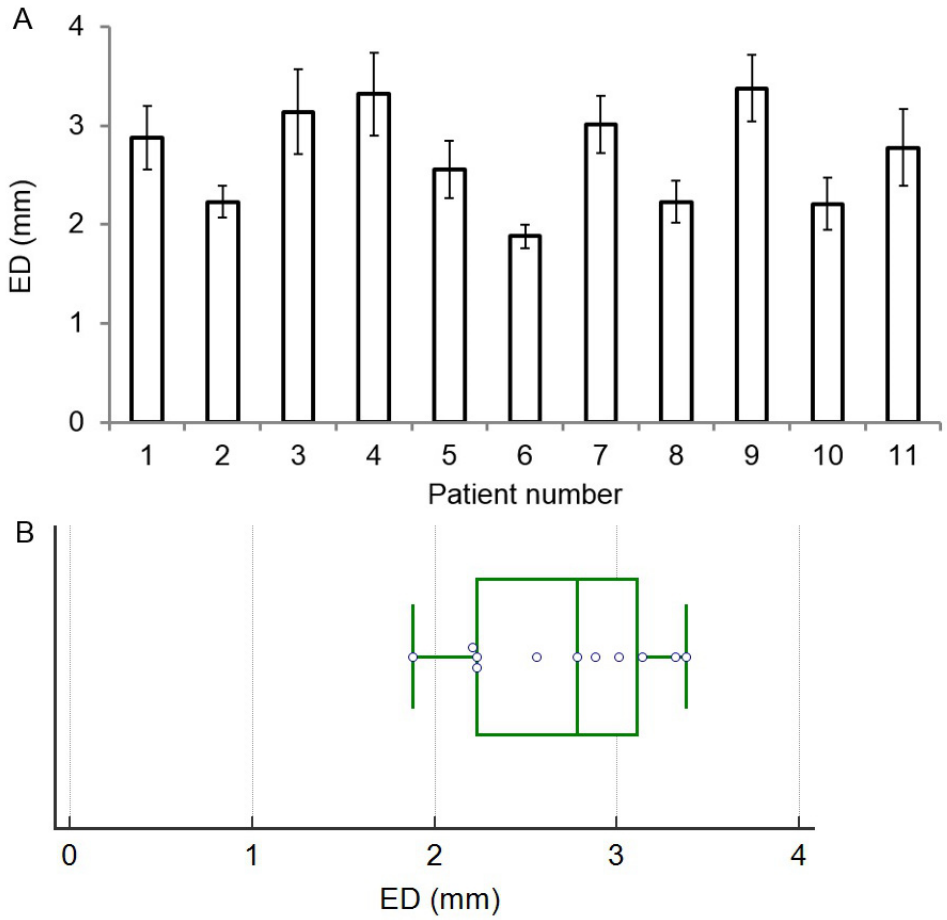

Figure 4: (A) Comparison of ED (in mm) and corresponding standard deviation for all the anatomical landmarks considered in all 11 patient datasets. (B) Box-and-whisker plot for the ED (in mm) for the11 patient datasets.

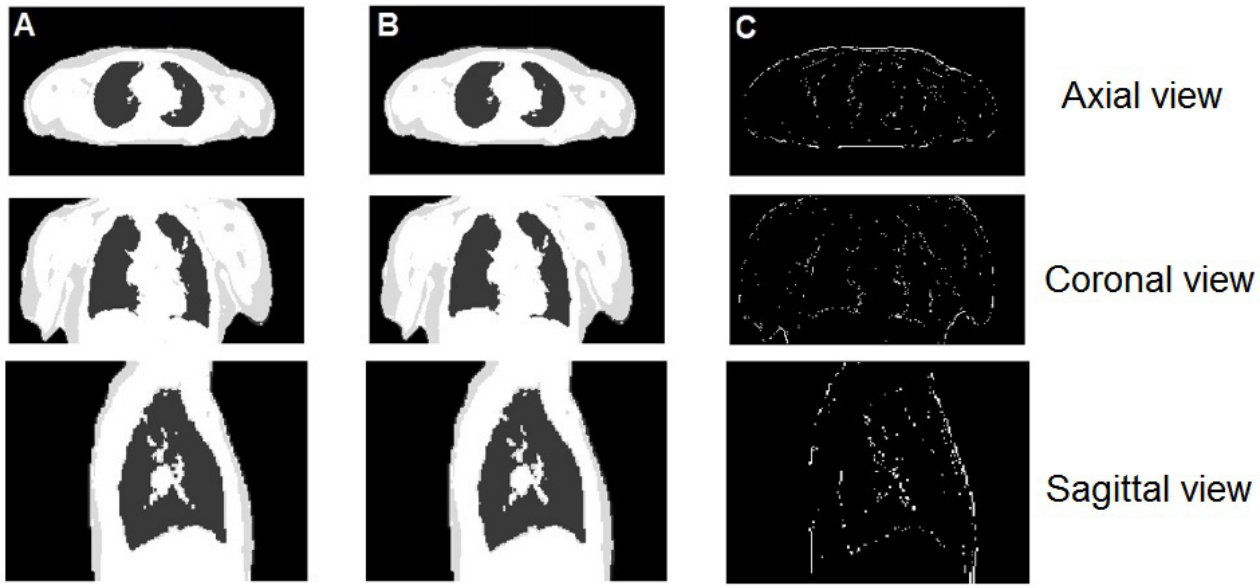

Figure 5: The axial, coronal and axial view of the (A) AM generated using our method based on a 4 tissue class attenuation model. (B) Corresponding 4D MR generated AM based on a 4 tissue class attenuation model. (C) Difference image between the two AMs.

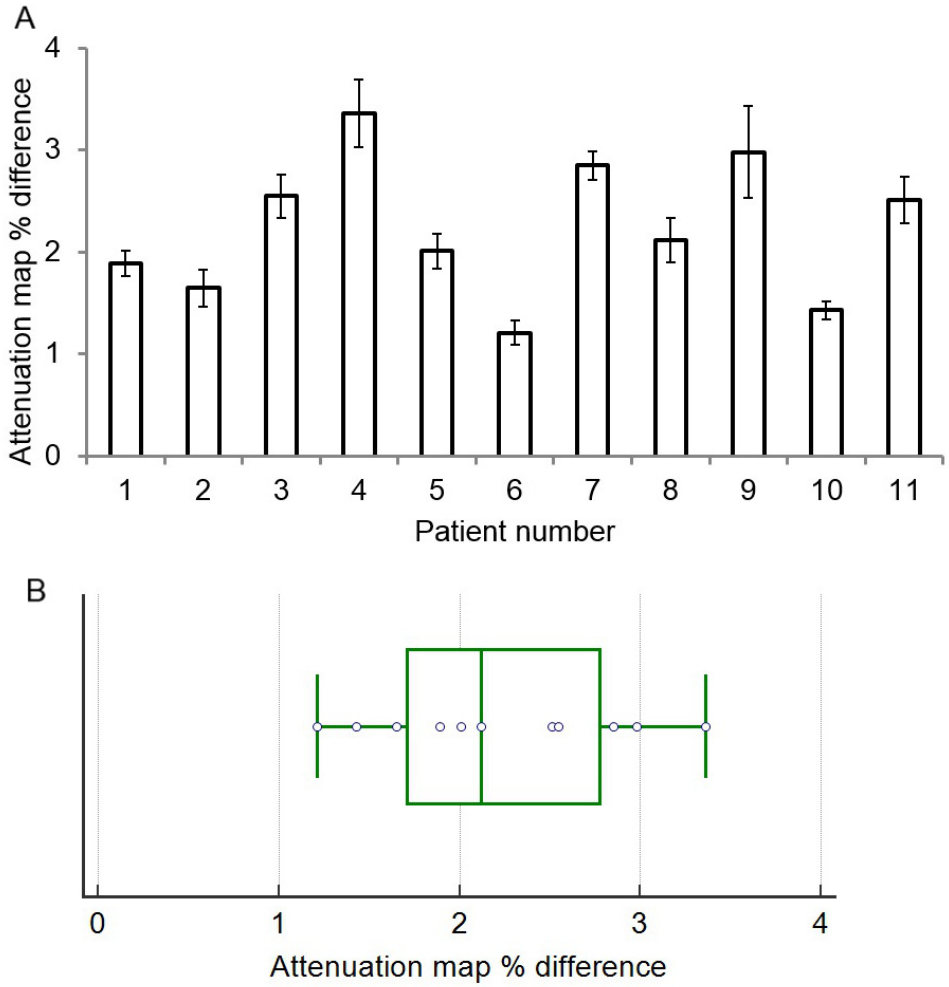

Figure 6: (A) AM percentage difference and corresponding standard deviation for all 11 patient datasets. (B) Box-and-whisker plot for the AM percentage difference for all 11 patient datasets.

Table 1

An overview of the patient demographics, including lesion and associated motion characteristics.

Patient	Age (y)	Sex	Type of malignancy	Lesion location	Volume (cm^3)*	Lesion displacement (mm)*
P1	67	M	Bronchial carcinoma	Lymph node, hilar	0.44	5.1
P2	61	M	Gastrointestinal stromal tumor	Stomach	1.80	7.4
P3	70	M	Bronchial carcinoma	Lung, lower lobe	0.97	16.2
P4	56	M	Nasopharyngeal carcinoma	Spleen	1.16	9.3
P5	32	F	Sigma carcinoma	Spleen	1.65	13.7
P6	69	M	Bronchial carcinoma	Lung, lower lobe	0.34	13.5
P7	62	F	Laryngeal carcinoma	Lung, middle lobe	0.58	5.6
P8	60	F	Bronchial carcinoma	Lung, lower lobe	0.31	7.4
P9	49	M	esophageal carcinoma	Middle thoracic esophagus	1.27	7.8
P10	54	M	Bronchial carcinoma	Lung, lower lobe	0.53	10.4
P11	52	F	Sigma carcinoma	Lung, lower lobe	0.66	11

* Determined using manual selection by an experienced radiologist on 4D-MR images

Table 2

Correlation coefficients between acquired and generated MR images for the 11 patients included in this study. The mean ± standard deviation corresponds to the three predicted volumes for each patient.

Patient number	CORRELATION COEFFICIENT (Mean ± Standard deviation)
1	0.954 ± 0.013
2	0.963 ± 0.021
3	0.927 ± 0.037
4	0.892 ± 0.035
5	0.915 ± 0.026
6	0.981±0.007
7	0.921±0.019
8	0.892±0.034
9	0.924±0.029
10	0.912±0.027
11	0.948±0.012

Table 3

Correlation coefficients between AMs generated using our method and the corresponding ones extracted from the 4D MR series for the 11 patient included in this study. The mean ± standard deviation corresponds to the three predicted volumes for each patient.

Patient number	CORRELATION COEFFICIENT (Average ± Standard deviation)
1	0.982 ± 0.007
2	0.978 ± 0.011
3	0.955 ± 0.016
4	0.876 ± 0.042
5	0.909 ± 0.033
6	0.973±0.012
7	0.928±0.023
8	0.937±0.031
9	0.887±0.04
10	0.891±0.025
11	0.934±0.022